# Composite SiN Foils for Suppression of $^{10}$B in Beryllium Accelerator Mass Spectrometry

M.Sc. Thesis in Physics

Benedikt. Þ. Kristinsson

202006628

*Supervisor:* Jesper Olsen

University of Aarhus

Department of Physics and Astronomy

June 15, 2022

# Contents

# Chapter 1

# Introduction

For centuries, scientists have sought to determine the age of ancient objects, geological formations, and even the Earth itself. One of the most famous methods developed for this purpose is radiocarbon dating, which leverages the decay of $^{14}$C to estimate the age of organic material. This method relies on the predictable decay of carbon isotopes over time, which can be modeled using differential equations. However, carbon dating is limited to relatively recent samples (up to about 50,000 years), and its effectiveness diminishes with age [1].

To extend dating beyond this range, scientists have turned to alternative methods that rely on cosmogenic isotopes, which offer longer half-lives and are suitable for much older materials. Due to the limitations of radiocarbon dating, alternative methods using cosmogenic isotopes such as $^{10}$Be have been developed

As the need for dating materials beyond this range grew, scientists turned to other isotopes for the precision dating of older objects. Among these, cosmogenic isotopes like $^{10}$Be have become invaluable, especially in geology, environmental science, and archaeology fields. $^{10}$Be, produced by cosmic rays interacting with the Earth's atmosphere, is particularly useful for dating ice cores, sediments, and other geological records, providing insights into long-term climatic and environmental changes.

A critical advantage of $^{10}$Be dating is its long half-life of approximately

$t_{1/2}$= 1.387 ± 0.0012Ma [2, 3], which allows us to study much older samples than with carbon dating. However, the long half-life of $^{10}$Be presents a detection challenge, as traditional decay counting methods are impractical due to low decay rates

The gamma-less beta decay of $^{10}$Be has a maximum energy of only 556 keV, which makes decay counting impractical for most natural samples [4]. The low-energy beta particles are difficult to detect, especially in complex samples with low $^{10}$Be concentrations, requiring more advanced techniques.

To address this challenge, Accelerator Mass Spectrometry (AMS) has emerged as a powerful method for detecting and analyzing cosmogenic isotopes like $^{10}$Be. AMS allows us to measure isotopic ratios with high precision, even in microscopic samples, by directly counting the number of $^{10}$Be atoms rather than relying on decay counting. However, AMS-based detection of $^{10}$Be faces a unique challenge.

The interference from isobaric ions like $^{10}$B which share the same mass number but differ in their nuclear properties. These nuclei have distinct isospin projections, reflecting their differences in nuclear structure despite their shared mass number, making it crucial to employ advanced techniques for effective separation and identification.

Differentiating these ions is crucial for accurate measurements, and while methods like degrader foils and gas-filled detectors have been used, they often come with trade-offs in efficiency and background suppression.

Recent innovations, such as the technique introduced by Steier et al. (2019), offer a promising solution.

By using a composite silicon nitride (SiN) foil stack, they have demonstrated an effective way to separate $^{10}$Be from $^{10}$B at higher acceleration potentials. This thesis aims to explore whether this method can be applied at lower voltage settings (1 MV), making it feasible for smaller AMS facilities, such as AARAMS. If successful, this technique could improve both the efficiency and accuracy of $^{10}$Be analysis, broadening the accessibility of high-precision dating methods to more laboratories around the world.
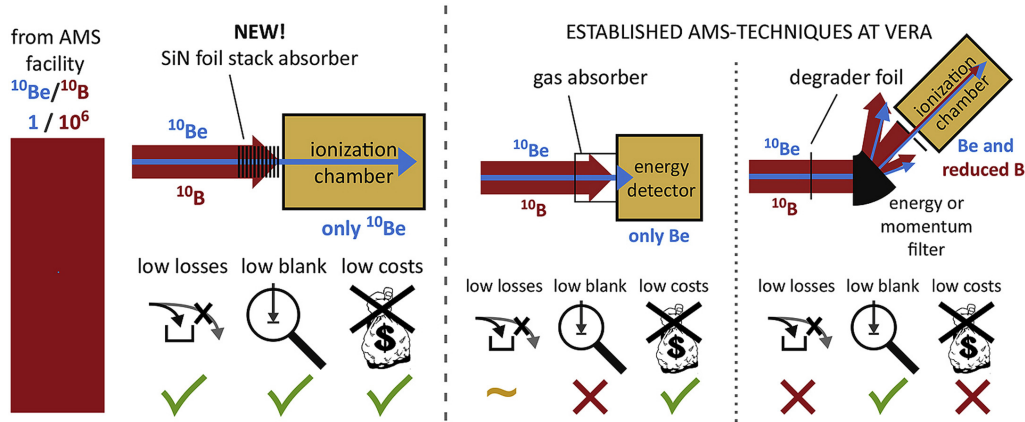
**Figure 1.1:** Comparison of separation methods in AMS, highlighting the new SiN foil stack absorber technique from Ref [5].

## 1.1   Thesis Structure

The necessary theoretical framework will be introduced, including some sections that are more relevant to this thesis's motivation and the understanding of the setup for the suppression of $^{10}$B in $^{10}$Be AMS measurements.

The experiment's methodology will be introduced, explaining the setups used for the experiments, the corresponding procedures, and the necessary framework for the SRIM simulations, which will be employed to model ion interactions and predict the stopping power and range of ions in the materials involved.

The analysis and discussion will then focus on the experimental results and the general efficiency of the two experimental setups, as well as a proof of concept for the suppression of $^{10}$B using SiN stack foils.

Finally, the analysis and discussion will be summarized.

# Chapter 2

# Theory

This chapter introduces the necessary theoretical background to understand the work done in this thesis.

## 2.1 Principles of AMS

This section is based on Refs.[6] and [7]. The general equipment layout for AMS and the process is illustrated on fig. 2.1 and this section will explain the theoretical knowledge needed to understand the fundamental processes in AMS.

To understand how AMS can separate isotopes with high precision, we first examine the core components of the system.
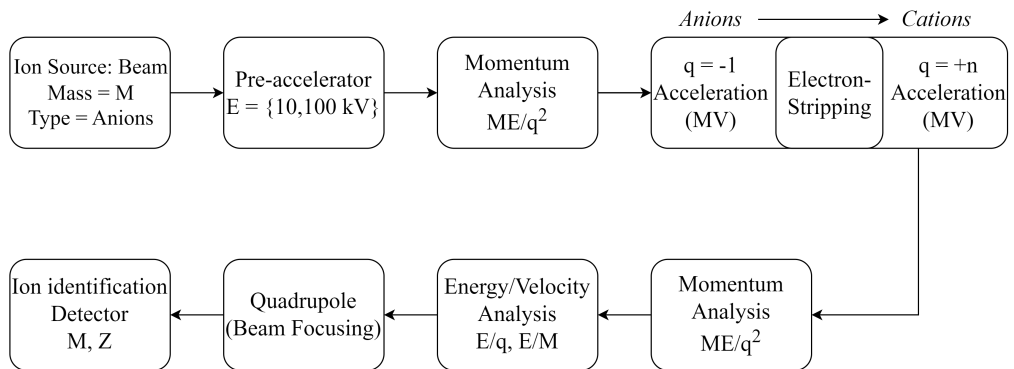
**Figure 2.1:** Schematic layout of equipment for AMS based on Ref.[7].

## Ion Sputter Source

An AMS sputter source typically consists of a system with a heated Cs reservoir, where Cs vapor is maintained at a pressure of approximately $10^{-4}$ mbar. This vapor is pumped into a cavity (see fig. 2.2). The cavity, which includes the ionizer, is constructed from a metal with a low work function, such as tantalum, tungsten, or molybdenum. The low work function refers to the energy required to remove an electron from the metal's interior to a point just outside its surface. This area is heated to 1000 Celsius to thermally ionize the Cs into $Cs^+$ (Cations). The symmetry of the cavity is constructed so that the $Cs^+$-ions are focused to hit the sample target - with their newly gained energy by applying an electric potential between the ionizer and the sample target - and ejecting atoms from its surface.

The applied voltage will dictate whether it's negative (Anions) or positive (Cations) ions we want to extract and further accelerate away from the ion source. The applied voltage determines whether the extracted ions are negative (anions) or positive (cations). The total energy of an emitted ion is given by:

$$E_{source} = eq(U_{ex} + U_{tar}) \tag{2.1}$$

where $e$ is the elementary charge and $q$ is the charged state [6].

## Magnets

The beamline of $Ce^-$ has a charge of $q = -1$, and therefore, a field is needed if they are to be moved along the AMS setup. Commonly known as a bending/injection (BI) magnet used for moment analysis, it is used to steer the beamline of $Cs^-$ into the correct path, particularly as it enters or is injected into the accelerator.

When a charged particle moves perpendicular to a magnetic field, it experiences a magnetic force that causes it to move in a circular trajectory.
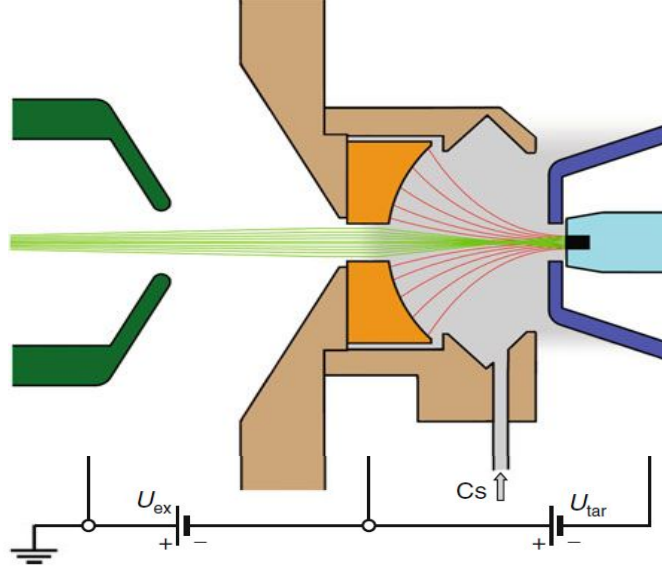
**Figure 2.2:** A generalized schematic of an ion sputter source for generating negative ions. Cs vapor is produced and introduced into the ion source via a tube (gray arrow). On the heated surfaces of the ionizer (orange), Cs atoms are ionized (red lines), which are focused onto the sample (black) within the metal target (cyan) by the target voltage ($U_{tar}$). As the $Cs^+$ ions sputter the target, negative carbon ions, $Cs^-$, (light green) are generated and then accelerated by $U_{tar}$, followed by the extraction voltage ($U_{ex}$).

The force due to the magnetic field provides the centripetal force necessary for this circular motion. By equating the centripetal force with that of the Lorentz force equation, $F = qvB$, and utilizing the kinetic energy and velocity of the charged particle - $E_{kin} = E_{source} = \frac{1}{2}Mv$ and $v = \sqrt{\frac{2E_{kin}}{M}}$ respectively. For an ion, $X(q,p)$, with charge $q$ and momentum $p = \sqrt{2 \cdot A \cdot E}$ in a homogenous magnetic field, $B$ the radius, $r$, of the curvature of its trajectory can be determined by analyzing these relationships yielding

$$\left(\frac{M}{q}\right)\left(\frac{E_{kin}}{q}\right) = k_1(Br)^2 \tag{2.2}$$

An energy/velocity analyzer is often placed post-acceleration of the beamline and is also known as an ESA. ESA is an instrument that uses

electric fields to separate charged particles (ions) based on their energy per charge. The force on a charged particle in an electrostatic field

$$F = q\mathcal{E} \tag{2.3}$$

can be used with the work-energy theorem to determine the trajectory of the curvature imposed by the electrostatic field

$$\frac{E}{q} = k_2\mathcal{E}r. \tag{2.4}$$

The charged ions' Lorenz force will cause the beamline to start spreading. Quadrupoles are utilized to gather the beamline.

## Tandem-Accelerator

A tandem accelerator utilizes a two-stage acceleration process, which involves converting negative ions into positive ions. The device accelerates ions through an electric potential difference, which is achieved by creating a high-voltage terminal at the midpoint of the accelerator. This allows for efficient acceleration of particles to higher energies.

In the first stage, negative ions are injected into the accelerator with an initial energy $E_i = V_i e$, where $V_i$ is the injection voltage and $e$ is the electronic charge. As the negative ions are accelerated towards the high-voltage terminal, they pass through an electron stripper. The electron stripper removes electrons from the negative ions, converting them into positive ions with charge $q$, typically resulting in a higher charge state.

After passing through the electron stripper, the now positive ions are further accelerated by the terminal's high-voltage potential $V_t$. This results in an increase in the kinetic energy of the ions.

The total energy $E_f$ of the ions after acceleration is given by:

$$E_f = E_i + (q + 1)eV_t \tag{2.5}$$

This equation shows that the final energy depends on the ions' initial energy and the terminal voltage.

For a more generalized expression of the ion energy $E$ after acceleration in the tandem, we can use:

$$E = \left( \frac{(V_i + V_t)M_p}{M_i} + qV_t \right) e \qquad (2.6)$$

Where $V_i e$ is the initial energy of the injected ions, $V_t$ is the terminal voltage, $e$ is the electronic charge, $q$ is the charge state of the ions after stripping, $M_p$ is the mass of the positive ion, and $M_i$ is the mass of the negative ion.

## 2.2 Isosbar

## 2.3 Cosmogenic Nuclide Dating

**Nuclear reactions**

**Nuclear Decay**

## 2.4 Stopping Power

# Chapter 3

# Methodology

## 3.1 AMS at Aarhus University

When measuring isotopic ratios of stable nuclei, such as isotopes, conventional mass spectrometry is sufficiently proficient, providing adequate sensitivity Refs. [8], [7].

This section describes the setup of AMS at AARAMS, covering the ion source, beamline, acceleration process, and detection system.

However, to measure cosmogenic nuclei such as $^{10}$Be, with isotopic ratios between $10^{-10}$ and $10^{-14}$, the limitations of conventional mass spectrometers are surpassed. Utilizing AMS allows access to higher energies, which in turn helps resolve ambiguities in identifying nuclei, atoms, and molecular ions of the same mass. As described in the section Principles of AMS, the setup at Aarhus University follows a similar configuration. The AMS system for AARAMS is composed of several components, which will be described in this section along with their effects on the ion beam. The schematic layout of AARAMS, depicted in fig. 3.1, shows that it can be divided into five "main" sections: Ion source, Low Energy section (LE), 1 MV accelerator, High Energy section (HE), and the Rare Isotope section (RI), followed by the detector.
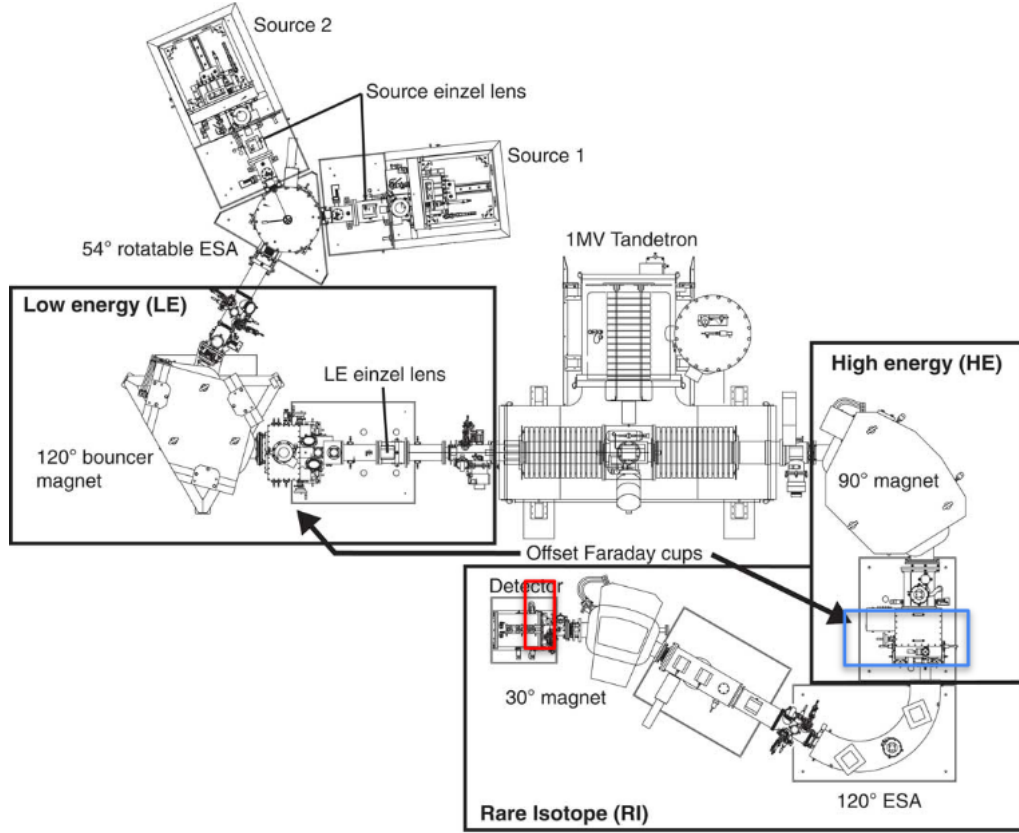
**Figure 3.1:** A 5-sub division of the 1 MV Tandetron Accelerator layout at Aarhus University Ref.[9]. The blue rectangle is where foils can be slit down to intersect the beam. The red rectangle is where we will add SiN foils, as suggested by Ref. [5]. The latter rectangles represent two different setups.

Additionally, the optical beam-handling components include Einzellenses, Y- and X-steerers, X-slits, apertures, Q-snout lenses, and Q-pole lenses, as well as retractable Faraday cups for measuring and analyzing the beam current.

## Ion Source

The first section in the AARAMS is essentially where the beam of $^{10}$Be, and other ions, is created. Inserting $^{10}$Be directly for analysis is not possible, due to its extremely low abundance, as well as doing so will contaminate the beam. The samples used are cathodes made out of copper - due to its electron

affinity of 118.4 $\frac{\text{kJ}}{\text{mol}}$ Ref.[10]- containing on average $0.7142 \pm 0.0761\,\text{mg}$ $^{10}\text{Be}^{16}\text{O}$, beryllium oxide, which is sometimes referred to as "beryllia" see table 3.1. Table 3.1 summarizes the batch information for the 10Be samples used in this study. The average weight of BeO was calculated using:

$$\text{Average BeO mass} = \frac{\sum \text{BeO weights}}{N} \quad (N = 12) \qquad (3.1)$$

where $N$ is the total number of samples. The uncertainty was calculated using the standard deviation $s$ of the weights:

$$s = \sqrt{\frac{\sum(x_i - \text{average})^2}{N-1}} \quad \text{and} \quad \text{Uncertainty} = \frac{s}{\sqrt{N}} \qquad (3.2)$$

Similar calculations are done for Niobium yielding an average mass of $m_{\text{Nb}} = 3.585 \pm 0.253\,\text{mg}$.

**Table 3.1:** $^{10}$Be Batch Information

| Sample Name mixing-ratios | Sample Type | Batch | Sample origin | Description of Carrier | Preparation Lab | Lab prep | Registration date | BeO mass (mg) | Nb added (mg) |
|---|---|---|---|---|---|---|---|---|---|
| AU2406 4.5 | pblk | AU2406 | MFK/Katya | PHE1603 | AARGEO | BE | 9/17/2024 | 0.62 | 2.81 |
| RUB20 4.1 | sam | AU2406 | MFK/Katya | PHE1603 | AARGEO | BE | 9/17/2024 | 1.35 | 5.53 |
| RUB21 8.5 | sam | AU2406 | MFK/Katya | PHE1603 | AARGEO | BE | 9/17/2024 | 0.27 | 2.29 |
| RUB22 4.2 | sam | AU2406 | MFK/Katya | PHE1603 | AARGEO | BE | 9/17/2024 | 1.07 | 4.51 |
| RUB23 5.3 | sam | AU2406 | MFK/Katya | PHE1603 | AARGEO | BE | 9/17/2024 | 0.76 | 4.00 |
| RUB24 4.2 | sam | AU2406 | MFK/Katya | PHE1603 | AARGEO | BE | 9/17/2024 | 0.79 | 3.28 |
| RUB26 5.2 | sam | AU2406 | MFK/Katya | PHE1603 | AARGEO | BE | 9/17/2024 | 0.72 | 3.77 |
| RUB27 4.3 | sam | AU2406 | MFK/Katya | PHE1603 | AARGEO | BE | 9/17/2024 | 0.79 | 3.43 |
| RUB28 4.0 | sam | AU2406 | MFK/Katya | PHE1603 | AARGEO | BE | 9/17/2024 | 0.73 | 2.95 |
| RUB29 4.0 | sam | AU2406 | MFK/Katya | PHE1603 | AARGEO | BE | 9/17/2024 | 0.93 | 3.72 |
| Cosmo1 4.7 | sam | AU2406 | MFK/Katya | PHE1603 | AARGEO | BE | 9/17/2024 | 0.60 | 2.84 |
| C0-34 4.9 | sam | AU2406 | | PHE1603 | AARGEO | BE | 9/17/2024 | 0.57 | 2.80 |

The type of ion source used at the AARAMS is a cesium sputter source, as described above. The AARAMS has two independently operable negative ion sources, HVEE SO-110C-1 (source 1) and SO-110C-2 (source 2), each capable of holding up to 50 samples. This allows for a quick switch between samples, which is admirable.

At AARAMS, cesium vapor is first heated to approximately $115\,^\circ\text{C}$ in a boiler and directed into an ionization cavity maintained at around $1000\,^\circ\text{C}$,

enabling efficient ionization because of cesium's low first ionization energy out of all the elements Ref.[11]. The cavity's ionizer, heated to $1100\,°\mathrm{C}$ by passing a current of approximately $18\,\mathrm{A}$ through an embedded coil, releases electrons, which interact with cesium atoms to create Cs+ ions. The generated cations are focused and accelerated towards the sample containing BeO to sputter its surface, creating a beam of anions. The adjustable length of the sample holder allows for precise positioning of the sample relative to the focal point, optimizing sputtering efficiency. At AARAMS, the target voltage and extraction voltage sum are set to $35\,\mathrm{kV}$, with a constraint of $\pm\,3\,\mathrm{kV}$ due to limitations in the bouncer injector magnet.

The beam of anions, consisting of molecules such as $^{10}\mathrm{Be}^{16}\mathrm{O}^-$, is subjected to uniform acceleration, resulting in equal kinetic energy for each ion. This ensures that all ions in the beam, regardless of their mass or charge, attain the same kinetic energy under these conditions. They are accelerated towards a rotatable ESA.

The ESA is a $54\,°$ electrostatic analyzer with a radius of $469\,\mathrm{mm}$, a gap of $53\,\mathrm{mm}$, and an energy-to-charge ratio of $44\,\mathrm{kV}$ [12]. The ESA can be seen in fig. 3.2, where two curved, parallel conducting plates create a radial electric field of strength $\mathcal{E}$ between them.

The ESA guides ions along a circular path, allowing only those with specific energy levels to pass through by setting the arc radius, $r$, according to the ions' energy-to-charge ratio, as described in eq. (2.4). The electrodes are held at equal voltages but with opposite polarities [12]. Given the electrostatic rigidity of an ion, $e$, the required voltage on one of the ESA electrodes can be calculated as:

$$\mathcal{V}_{ESA} = \frac{E_i\, x_{\mathrm{gap}}}{q\, r} \tag{3.3}$$

where the ion's energy, $E_i$, the gap between the electrodes, $x_{\mathrm{gap}}$, the ion's charge, $q$, and the radius of curvature, $r$, are used in the calculation.
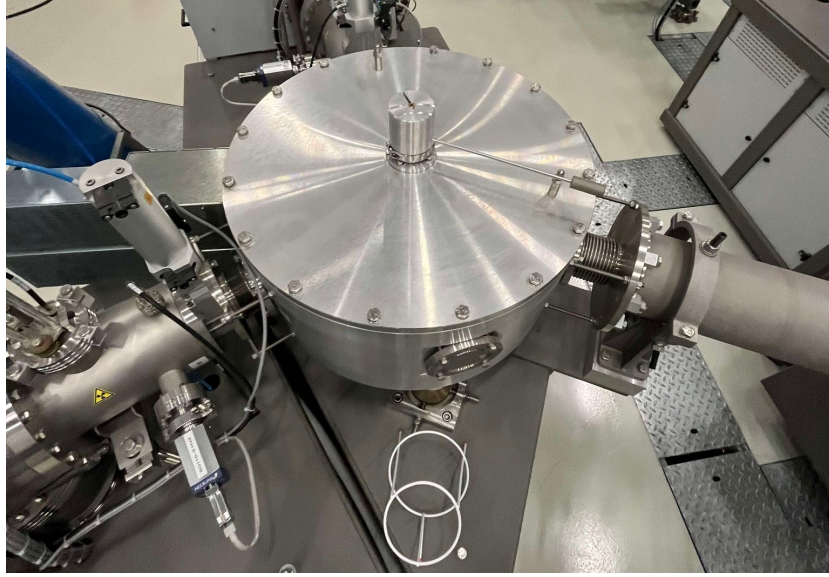
**Figure 3.2:** Rotatable 54° Electrostatic analyzer.

## LE section

In the LE section, ions are sorted and directed based on their energy and charge before entering the accelerator. The crucial elements here include the ESA and the bouncer magnet, which help separate and direct ion beams of different masses through the accelerator.

When the electrostatic rigidity of the ions has been adjusted by the ESA, the ion beam is guided through a $120\,^\circ$ bouncer magnet. The bouncer magnet, with a 455 mm radius and a gap of approximately 62 mm. By controlling the magnetic rigidity whose ratio is given by eq. (2.2), the trajectory of the charged particles in the ion beam will be determined.

To ensure that ion beams of different masses follow the same trajectory through the bouncer magnet, we must adjust the bouncer voltage, ensuring the same magnetic rigidity for all ions in the beam. This is crucial because beams of differing masses would otherwise follow different paths in the BI magnet. The relationship between two ion beams, one of a reference mass and the other of a different mass, is governed by the equality in their magnetic rigidity this could be for $^9$Be and $^{10}$Be

$$\frac{p\left({}^{9}\text{Be}\right)}{q\left({}^{9}\text{Be}\right)} = \frac{p\left({}^{10}\text{Be}\right)}{q\left({}^{10}\text{Be}\right)}$$

and by substituting the momentum as defined in section 2.1 allows us to determine how the bouncer voltage should be adjusted to ensure the same path for both beams

$$\sqrt{\frac{2m_9 E_9}{q\left({}^{9}\text{Be}\right)^2}} = \sqrt{\frac{2m_{10} E_{10}}{q\left({}^{10}\text{Be}\right)^2}} \tag{3.4}$$

This equation can be used to tune the bouncer voltage settings such that ion beams of different masses, ${}^{9}$Be and ${}^{10}$Be, will leave the bouncer magnet following the same trajectory.

**Hall effect and magnetic monitoring**

To ensure precise magnetic control, the system uses Hall probes, which measure the field strength based on the Hall effect. To ensure precise control of the magnetic field in the bouncer magnet, the system at AARAMS employs Hall probes. These are calibrated sensors that utilize the Hall effect to monitor the strength of the magnetic field within the magnet. The Hall effect occurs when a magnetic field is applied perpendicular to a current flowing through a conductor, causing a Lorentz force to deflect the electrons and accumulate charge on one side of the conductor. This accumulation results in a voltage difference, called the Hall voltage, which is proportional to the magnetic field strength [13, 14].

The Hall voltage $V_H$ is given by

$$V_H = \frac{IB}{ned_c} \tag{3.5}$$

where $I$ is the current through the conductor, $B$ is the magnetic field strength, $n$ is the charge carrier density, $e$ is the electron charge, $d_c$ is the thickness of the conductor.

By continuously measuring the Hall voltage, we can monitor the magnetic field in real-time, ensuring that it remains at the correct strength to direct the ion beam along its intended trajectory. This is particularly important for ensuring that the beam of ions, such as $^9$Be and $^{10}$Be, is precisely focused as it exits the bouncer magnet and proceeds to the accelerator.

To match the trajectory of beams with different masses, the bouncer voltage $V_{\text{BNC}}$ must be tuned accordingly. The reference beam, with mass $m_{\text{REF}}$, has a reference bouncing voltage $V_{\text{REF}}$, which is typically set to zero. For a beam of mass $m_{\text{BNC}}$, the energy equation can be expressed as:

$$m_{\text{BNC}}q(V_{\text{Tar}} + V_{\text{Ex}} + V_{\text{BNC}}) = m_{\text{REF}}q(V_{\text{Tar}} + V_{\text{Ex}} + V_{\text{REF}}) \qquad (3.6)$$

Isolating for $V_{\text{BNC}}$, we get:

$$V_{\text{BNC}} = (V_{\text{Tar}} + V_{\text{Ex}} + V_{\text{REF}})\frac{m_{\text{REF}}}{m_{\text{BNC}}} - (V_{\text{Tar}} + V_{\text{Ex}}) \qquad (3.7)$$

This equation determines the bouncer voltage necessary to ensure that beams with different masses follow the same trajectory through the bouncer magnet, allowing for precise acceleration and injection into the accelerator [12].

# 1 MV Accelerator Section

Figure 3.3 provides a view of the 1 MV tandem accelerator at AARAMS, highlighting the entry point for the cation beam, which has been sorted by energy, charge, and mass.

To understand the accelerator at AARAMS, it is important to be familiar with its main components: an insulating tank filled with $SF_6$ gas, low- and high-energy accelerator tubes, a Cockcroft-Walton voltage multiplier, and a charge-exchange chamber equipped with gas, pressure gauges, and various beam-handling elements, including Q-snout and Q-pole lenses. This section plays a critical role in determining the charge state and energy distribution of ions as they move toward the FC and detector. At the core of the AARAMS
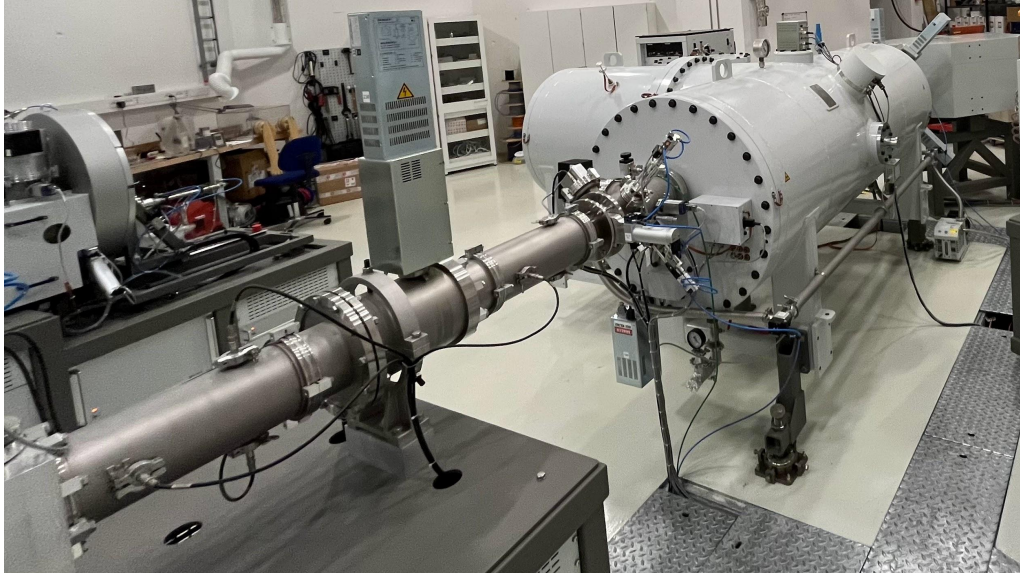
**Figure 3.3:** The 1 MV tandem accelerator at AARAMS, showing the entry pipe where the ion beam enters the accelerator.

accelerator lies a gas-exchange tube, commonly referred to as the "stripper," which enables dual acceleration of ions within a single voltage potential.

The stripper dissociates complex molecular ions, such as $BeO^-$, reducing their intensity and converting anions into cations. This process allows smaller molecular fragments to be filtered out in subsequent stages, though it typically reduces the overall beam intensity [15].

At the center of the accelerator chamber, the terminal acceleration potential is generated by a Cockcroft-Walton (CW) multiplier, which is schematically depicted in fig. 3.4.

The CW multiplier converts a low AC input to a high DC output by employing a sequence of diodes and capacitors, which sequentially step up the voltage. This design ensures a stable and high terminal voltage for ion acceleration. In the CW multiplier, each of the N stages consists of two capacitors and two diodes. The capacitors are charged in parallel, with every second capacitor in each stage connected in series between the ground and the output. This configuration results in an output voltage proportional to the number of stages, effectively multiplying the input voltage by an even
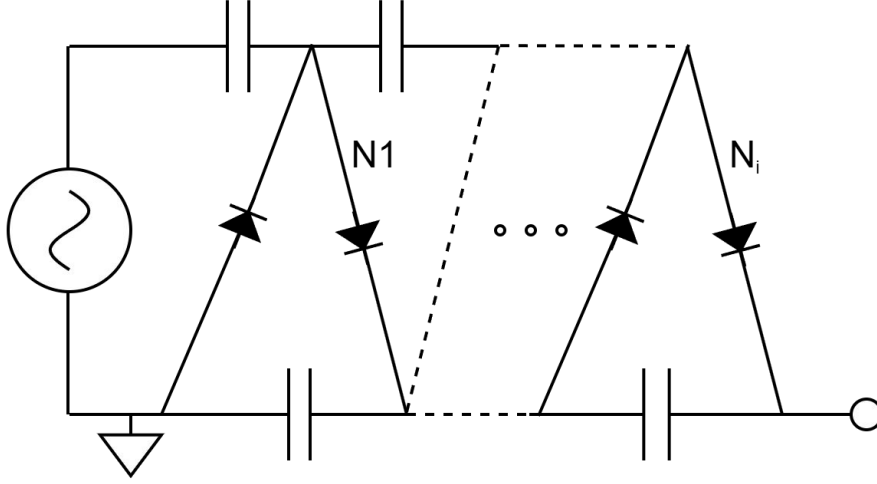
**Figure 3.4:** Circuit diagram of an N-stage Cockcroft-Walton multiplier, inspired by Refs. [16] and [17].

factor.

The output voltage, $V_{out}$, is therefore given by:

$$V_{out} = 2N_i V_{in} \tag{3.8}$$

where $N_i$ is the number of stages and $V_{in}$ is the input voltage.

This terminal voltage creates the electric field that drives ion acceleration throughout the system, with field strength gradually decreasing at the extremities of the accelerator.

## Charge-exchange gas cell

At AARAMS, the gas used in the stripper is typically argon, with the option to switch to helium via the dual gas stripper setup [18]. Gas is preferred in the stripper to ensure stable beam transmission, especially when lower charge states are desired. In the stripping process, the negative ion beam is directed through a gas layer with a thickness of approximately $1 - 2\,\mu\text{g/cm}^2$, while minimizing gas diffusion into the low- and high-energy accelerator tubes. Excessive gas in these tubes can scatter the ion beam,

potentially producing neutral particles, positive ions, and electrons that
disrupt transmission efficiency, particularly if the vacuum is suboptimal. The
low-energy tube is more susceptible to such interference, as the slower ions
here are more prone to charge exchanges outside the stripper. To mitigate
these issues, turbopumps maintain a high vacuum in the tubes, recirculating
gas back to the stripping chamber.

If electrons produced through scattering are not directed to a tube
electrode, they may gain enough energy to cause further collisions, leading
to additional electron or ion production. The resulting X-rays can ionize
the insulating gas, drawing charge from the multiplier and terminal rings
to the tank wall, leading to voltage drops, known as electron loading. To
control radiation levels, a bias ring set to $-4$ is placed at the accelerator
entrance to block incoming electrons.

In the LE section of the accelerator tube, ions reach a total energy at
the stripper defined by

$$E_{\text{strip}} = E_i + eV_{\text{TV}} \tag{3.9}$$

where $E_i$ is the initial ion energy, and $V_{\text{TV}}$ is the accelerator's terminal
voltage.

Upon entering the stripper, ions undergo two main processes: electron
capture, which decreases the ion's charge state q by one as an electron is
gained, and electron loss, where the ion loses an electron, increasing its
charge state. These processes are represented by the reactions:

$$Z^q + e^- \rightarrow Z^{q-1} \tag{3.10}$$

and

$$Z^q \rightarrow Z^{q+1} + e^- \tag{3.11}$$

Each process has a specific probability based on cross-section, ion charge,
excitation state, and kinetic energy. As ions move through the gas, they al-
ternate between capture and loss, stabilizing into a quasi-pseudo-equilibrium
charge state. This process allows various charge states for $^{10}$Be, such as
$^{10}$Be$^{q+1}$ and $^{10}$Be$^{q+2}$. Diagram illustrating the charge-exchange process for a

negative ion (q = -1) as it passes through a stripping gas or foil. A schematic of this is shown in fig. 3.5, the vertical axis represents the charge state, the left horizontal axis shows the thickness of the stripping medium in arbitrary units, and the right horizontal axis indicates the fraction of ions in each charge state that has passed through the stripper.
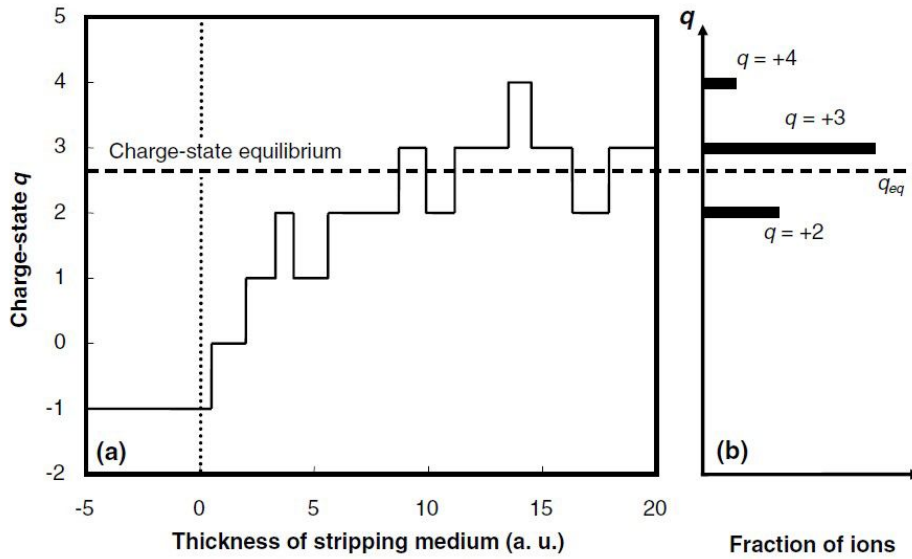


**Figure 3.5:** Stepwise exchange is shown schematically for an ion of charge $q = 1$ Ref. [19].

Although the stripper is a minor component of the AARASM, it plays a crucial role and requires precise handling. Stripper gas pressure is pivotal: it influences the efficiency of molecule ion dissociation but, if too high, may cause beam divergence due to angular scattering [12]. This effect can be mitigated to an extent by the Q-pole lens at the exit.

Optimizing the stripper gas cell pressure is essential to suppress unwanted background while maximizing the desired charge states of $^{10}Be^q$. However, specifying the exit charge state with complete certainty is challenging due to the energy-dependent charge state distribution and the quasi-pseudo-equilibrium state, along with unavoidable scattering events.

Because of the low nuclear physics energy regime, high charge states $q > 5$ are not abundant and thus not a primary concern.

Neglecting potential energy loss, the energy of positive ions leaving the accelerator remains as given in eq. (2.5).

Despite its critical function, the stripper poses challenges. Transmission measurements through the stripper are given as a function of thickness, $\mu g/cm^2$, rather than pressure, and the stripper tube's volume at AARAMS is unknown. To approximate thickness, we use the pressure gauges near the stripper to obtain terminal readings.

The stripper thickness can be calculated by integrating the local number density along the beam path:

$$d = \int_{-\infty}^{\infty} \mu(x)\,dx \qquad (3.12)$$

Assuming constant pressure throughout the gas cell, we can simplify the thickness calculation using the ideal gas law. However, this approach overlooks potential leakage at the ends. To account for this, we approximate the local number density by assuming a constant pressure inside the cell and a gradual pressure decay outside, proportional to the cell radius and inversely proportional to the square of the distance. Thus, the effective thickness is estimated as

$$d = A\frac{273.15}{273.15\,T(\,^{\circ}\mathrm{C})}\frac{P_G(\mathrm{torr})}{760}\left(\ell + 2(r_1 + r_2) + (\ell_1 - \ell)\frac{P_1}{P_G}\right) \qquad (3.13)$$

where $\ell, P_G, \ell_1, P_1$ denote the gas cell's length and pressure, and the first differentially pumped cylinder's length and pressure. The pressure $P_1$ is unknown due to the absence of a gauge at this location [20].

To use eq. (3.13), we make an educated estimate between the terminal pressure and the LE tube's endpoint pressure reading. Dimensions are available from diagrams, but the temperature inside the cell remains unknown, as AARAMS lacks an internal sensor.

During the accelerator's startup, the pressure in the $SF_6$-filled tank increases to steady-state due to heating from the Cockcroft-Walton multiplier. Assuming ideal gas behavior, the temperature increase can be calculated as follows:

$$\frac{P_i}{P_f} = \frac{T_i}{T_f} \qquad (3.14)$$

**Figure 3.6:** HE section at AARAMS from High Voltage Engineering Europa B.V.

where $(P_i, T_i)$ and $(P_f, T_f)$ represent initial and final pressures and temperatures. The initial tank temperature, assumed to match room temperature, is reasonable if the AMS system hasn't been active for an extended time.

## HE Section

The high-energy ion beam with energy given by eq. (2.6) leaves the accelerator. It now enters the 90 ° analyzing magnet, with a radius of 850 mm, a gap of 50 mm, and a mass-energy product of 63-73 AMU – MeV in the HE section. The 90 ° HE magnet is shown on fig. 3.6. The increased energy of the ion beam will now require the magnetic-, and electric fields in filtering components, e.g. ESA, to be stronger compared to the latter sections

The HE magnet analyzes the ion beam according to a radius that can be isolated from eq. (2.2).

Molecules such as $^{10}\text{Be}^{16}\text{O}$ will be dissociated in the stripper, and therefore the mass of some ions will have changed. The function of the magnet is to guide the trajectory of $^{10}\text{Be}$, as well as $^{10}\text{B}$, the $^9\text{Be}$ will be separated

and measured in offset Faraday cups after the magnet. The ion beam will continue toward the RI section. Additionally, the Faraday cup used to measure the $^9$Be$^+$-ion beam is equipped with two vertical slits (electrodes) that provide information about the beam's position within the cup. The signal generated by these slits can be utilized in a feedback loop to stabilize the terminal voltage of the accelerator, ensuring that the rare isotope beam enters the ESA in the RI section at a precisely defined and reproducible location Ref.[12]. This is illustrated in fig. 3.7 which is from Ref.[21].
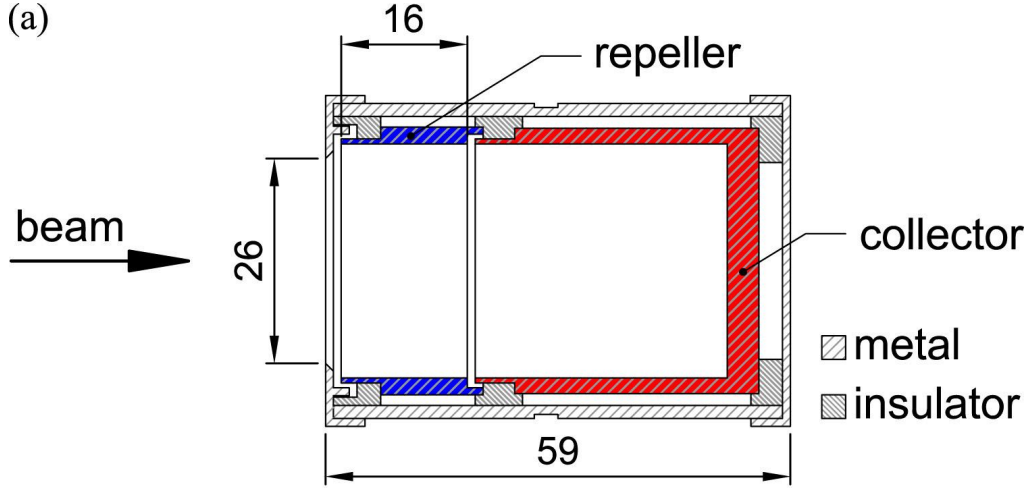


**Figure 3.7:** Standard Faraday cup utilized in REX-ISOLDE. Cross-sectional view of the standard REX-ISOLDE Faraday cup, with distances indicated in millimeters.

## RI Section

The last section before the detector is the rare-isotope section. The main components the ion beam will traverse are the 120 ° ESA and the 30 ° magnet before reaching the ionization chamber section (GIC).

We use an Electrostatic Analyzer (ESA) with a deflection angle of 120°, a radius of 650 mm, a gap of 25 mm, and an energy-to-charge ratio of 1.5 MV. Although this ESA removes many unwanted particles, some isobars may still

pass through due to their increased energies. To further refine the beam, it is directed through a second ESA before passing into a 30° magnet with a radius of 850 mm, a gap of 40 mm, and an energy-to-charge ratio of 63 AMU-MeV, with a maximum tolerance of 73 AMU- MeV. This additional magnetic filtering step ensures even greater suppression of background particles and unwanted ions that might have scattered off the ESA electrodes, enhancing the purity of the final beam.

## Detector

The detector is a gas ionization chamber filled with isobutane that operates as follows:

Upon entering the chamber through a thin foil-covered window, a beam of cations traverses the detector's gas volume. As the ions pass through the gas, they collide with isobutane molecules, losing energy until they come to a complete stop. This energy loss, referred to as the stopping power, is the key measurement of the detector and is expressed as the energy loss per unit path length - $\frac{dE}{dx}$.

Most of the ion energy is used to produce electron-ion pairs in the gas, a process called electronic energy loss, with a negligible fraction converted to thermal energy. This energy loss mechanism is described by the Bethe-Bloch equation [22], which models the electric field generated by a moving particle as follows:

$$E = \frac{Ze}{4\pi\epsilon_0}\frac{1}{b^2} \tag{3.15}$$

where $Z$ is the atomic number of the ion, $e$ is the elementary charge, and $b$ is the impact parameter. By integrating over all relevant impact parameters, we can calculate the total energy loss per unit length, by summing the energy transferred to electrons at various distances. If $n$ is the electron density in the isobutane, the number of electrons within a radius $b$ and thickness $db$ is $2\pi b\,db\,n$. Applying classical and quantum mechanical limits yields the following non-relativistic expression for the energy loss:

$$\left(\frac{dE}{dx}\right)_e = \frac{4\pi Z^2 e^4}{m_e v^2} n \ln\left(\frac{2m_e v^2}{I}\right) \tag{3.16}$$

where $v$ is the particle velocity, $v = c\sqrt{1 - (Ac^2/E + Ac^2)^2}$, $m_e$ is the electron mass, $c$ is the speed of light in vacuum, and $I$ is the mean excitation energy. In high-energy regimes, energy loss scales as $\frac{AZ^2}{E}$, while at low energies, incomplete stripping of the ion's electrons results in a decreasing $\frac{dE}{dx}$.

A schematic of the GIC is shown in fig. 3.8. As the ion beam travels through the gas, it splits isobutane molecules into electron-ion pairs, which are separated by an electric field, electrons drift toward the anodes and ions toward the cathode. The number of electron-ion pairs produced is proportional to the ions' energy loss.
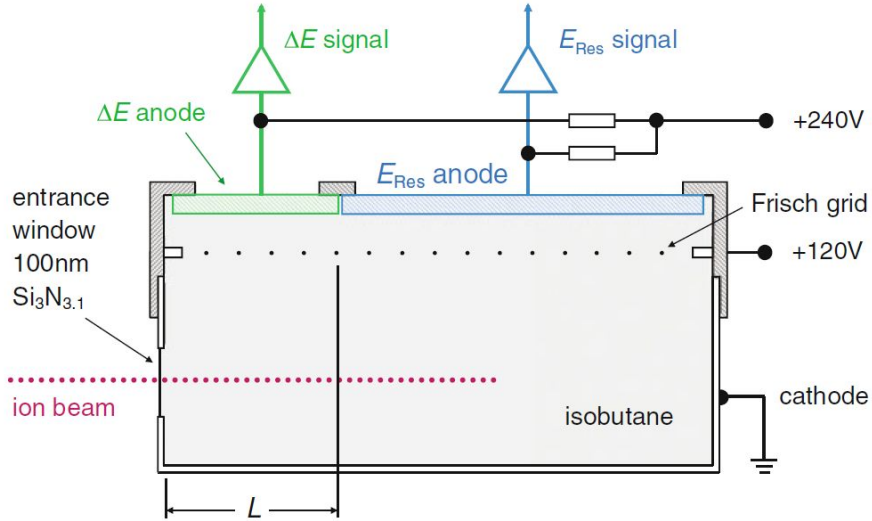


**Figure 3.8:** Schematic of an ionization chamber detector with a two-part anode, adapted from Ref [8]. Each section of the anode collects electrons from the sensitive volume beneath it. The $\Delta E$-anode's sensitive volume is defined by length $L$. A Frisch Grid is positioned between the ionization region and the anodes.

Due to their higher mobility, electrons reach the anodes faster than ions, which effectively makes ions appear stationary during electron collection.

The Frisch Grid, located between the anodes and the cathode, minimizes positional and drift velocity effects by allowing only electrons that pass through it to generate a signal on the anode.

The data acquisition system collects signals from the two anodes, $\Delta E$ and $E_{res}$, in a two-dimensional manner, amplifying each signal independently.

The detector is designed with electric fields perpendicular to the anodes, ensuring each anode collects electrons only from the volume directly below it. The signal from the first anode is proportional to the integral of the electronic energy loss over the length $L$:

$$\Delta E \propto \int_0^L \left(\frac{dE}{dx}\right)_e dx \qquad (3.17)$$

where $L$ is the length of the $\Delta E$ region along the beam direction. The second anode, long enough to capture all remaining ions, measures the residual energy:

$$E_{res} \propto \int_L^\infty \left(\frac{dE}{dx}\right)_e dx \qquad (3.18)$$

Simultaneous measurements of energy loss and residual energy enable the determination of an ion's nuclear charge $Z$, which varies for isobars like $^{10}$Be and $^{10}$B due to their differing energy loss profiles in isobutane.

The ideal length of the $\Delta E$-anode is set by identifying the crossing point in energy loss curves as a function of penetration depth for different ions. From these measurements, $\Delta E$ and $E_{res}$ can be obtained by analyzing intersections in energy loss curves.

Differences in signal help distinguish between ions, depending on the detector's resolution and the applied energy.

The signal, displayed as energy, is typically recorded as a channel number, which can be calibrated for a known isotope, such as $^{10}$Be. To enhance the detection of $^{10}$Be, blank-$^{10}$Be samples can be measured as references.

A critical factor for detector performance is the isobutane gas pressure, as it affects both resolution and detection count. Pressure impacts the signals

recorded on each anode and influences ion separation. High pressure stops ions sooner under the first anode, potentially complicating ion differentiation, while low pressure may prevent full ion stopping, lowering the count. Optimal pressure is achieved when energy distribution between the two anodes is balanced for the isotope of interest.

## 3.2   Setups

As shown in [5], the overall ion detection efficiency for the degrader foil technique was 15%, approximately one-third of the 45% achieved with the SiN foil stack method. Building on this, we will determine the efficiencies of the degrader foil and SiN stack methods using our setup and compare their performance. We are interested in reproducing similar findings for the 1MV tandem accelerator at AARAMS, see table 3.2.

**Table 3.2:** A comparison of the performance parameters for the three isobar suppression methods used at VERA in $^{10}$Be detection. The overall ion detection efficiency refers to the detection efficiency from the anion beam in the ion source to the final $^{10}$Be detection, excluding the ionization yields of the sputter source.

| Parameter | Degrader Foil | Gas Absorber | Foil Stack |
|---|---|---|---|
| Overall ion detection efficiency | 15% | 5% | 5% |
| Stripping yield & acceler. transm. | 55% | 5% | 55% |
| HE-transm. & detector efficiency | 28% | >90% | >80% |
| Reproducibility for identical sputter targets, $^{10}$Be/$^{9}$Be $> 10^{-12}$ | 3% | 1% | 1% |
| Blank level $^{10}$Be/$^{9}$Be | $(2 + 4/-2) \times 10^{-16}$ | $1 \times 10^{-14}$ | $< 7 \times 10^{-16}$ |

**Degrader technique**

**Absorber technique**

## 3.3   Statistical Approach for Clustering and Outlier Detection

The analysis of these $^{10}$Be clusters uses a series of advanced statistical methods to identify and refine the region of interest (ROI) within a com-

plex dataset, specifically aimed at isolating and quantifying the signal of $^{10}$Be. The methodology followed a multi-step process, including K-Means clustering, silhouette scoring for model optimization, outlier detection, and re-clustering of the ROI. Below is a detailed breakdown of the statistical approach employed.

## K-Means Clustering for Data Grouping

The dataset was first subjected to K-Means clustering to identify natural groupings within the data. The K-Means algorithm is a partitioning method that iteratively assigns each data point to one of the $k$ clusters by minimizing the within-cluster variance. A range of $k$-values was evaluated to determine the optimal number of clusters. The silhouette score, which measures both the cohesion and separation of clusters, was used to identify the best clustering solution. The silhouette score is defined for each point and ranges from $-1$ to $+1$, with higher values indicating better-defined clusters.

## Outlier Detection and Filtering

Following the initial clustering, an important refinement step was undertaken to filter out outliers that could affect the precision and reliability of the $^{10}$Be counts. Outliers were detected using the Local Outlier Factor (LOF) algorithm, which evaluates the local density of data points and identifies points that are less dense compared to their neighbors [23]. The LOF algorithm operates as follows:

1. **Reachability Distance**: For a point $A$, the reachability distance to a neighbor $B$ is defined as:

$$\text{reachability-distance}_k(A, B) = \max\{k\text{-distance}(B), d(A, B)\},$$

   where $k$-distance$(B)$ is the distance to the $k$-th nearest neighbor of $B$, and $d(A, B)$ is the Euclidean distance between $A$ and $B$.

2. **Local Reachability Density (LRD)**: The LRD of $A$ is the inverse of the average reachability distance from $A$ to its $k$ nearest neighbors:

$$\text{lrd}_k(A) = \frac{|N_k(A)|}{\sum_{B \in N_k(A)} \text{reachability-distance}_k(A, B)},$$

where $N_k(A)$ is the set of $k$ nearest neighbors of $A$.

3. **LOF Score**: The LOF score for $A$ is computed as:

$$\text{LOF}_k(A) = \frac{1}{|N_k(A)| \cdot \text{lrd}_k(A)} \sum_{B \in N_k(A)} \text{lrd}_k(B).$$

A score close to 1 indicates that $A$ has a similar density to its neighbors, while $\text{LOF}_k(A) \gg 1$ suggests an outlier. Points with $\text{LOF}_k(A) > $ threshold were flagged as outliers and removed from the dataset.

**Re-clustering of the ROI**

To further refine the grouping of the ROI cluster, the filtered data points were re-clustered using K-Means with a reduced number of clusters. This step ensured that the ROI cluster remained well-defined and homogeneous after outlier removal.

## 3.4 Counting of $^{10}$Be - Blocks to Runs and Samples

At AARAMS, the SO110 ion source sample wheel can hold up to 50 samples, each of which undergoes multiple measurements called "runs." Each run consists of several measurement cycles, referred to as "blocks." The number of blocks per run is determined by stop conditions set in the Tandetron control software via a batch file. These conditions may be based on either a fixed number of blocks or a target count of rare isotopes (e.g., $^{26}$Al or $^{10}$Be). The choice of stop conditions depends on the required sample precision. Data analysis involves aggregating blocks into runs and averaging

the runs to determine sample means, which are reported as the final results of cosmogenic isotope analysis. This methodology follows the approach outlined in [24], where further details can be found.

## Blocks

A block represents a single measurement cycle where the ion beam interacts with the sample, and rare/stable isotope counts are recorded. The rare isotope ratio for a block is given by

$$R_{\text{Block}} = \frac{neq}{It}$$

where $n$ is the isotope count within the region of interest (ROI), $e$ is the elementary charge, $q$ is the ion charge state, $I$ is the stable isotope current (measured using Faraday cups), and $t$ is the detector live time. The uncertainty in block measurements is calculated as

$$\sigma_{R_{\text{Block}}} = \frac{eq}{It}\sqrt{n}$$

## Runs

A run consists of multiple blocks for a single sample. The number of blocks per run is determined by the AMS software stop conditions. The rare isotope ratio for a run is computed as a weighted average of block ratios:

$$R_{\text{run}} = \frac{\sum_i R_{\text{block},i} I_i t_i}{\sum_i I_i t_i}$$

where $I_i t_i$ represents the stable isotope charge, serving as the weighting factor. The error in the weighted average of block ratios is given by the maximum of the counting statistical error and the variance-based error:

$$\sigma_{R_{\text{Run}}} = \max\left[\sigma_{R_{\text{Run}}}^{\text{count}}, \sigma_{R_{\text{Run}}}^{\text{var}}\right] = \max\left[\frac{\sum_i \sigma_{R_{10,\text{block},i}} I_i t_i}{\sum_i I_i t_i \sqrt{n_{\text{block}}}}, \frac{\text{stdev}\langle R_{\text{block}}\rangle}{\sqrt{N_{\text{block}}}}\right]$$

## Samples

A sample measurement consists of multiple runs, and the sample ratio is computed as the weighted average of run ratios:

$$R_{\text{sample}} = \text{wavg}\langle R_{\text{run},x}\rangle$$

where the error is the maximum of the counting statistical error and the variance-based error:

$$\sigma_{R_{\text{Sample}}} = \max\left[\sigma_{R_{\text{Sample}}}^{\text{count}}, \sigma_{R_{\text{Sample}}}^{\text{var}}\right] = \max\left[\text{SE}\langle\sigma_{R_{\text{run},x}}\rangle, \frac{\text{stdev}\langle R_{\text{run},x}\rangle}{\sqrt{n_{\text{run},x}}}\right]$$

Strictly speaking, the distinction between counting statistics and sample variance applies when summarizing blocks into runs. When aggregating runs into sample means, the underlying runs may already include sample variance rather than counting statistics. However, this distinction is maintained here for clarity and consistency.

# Chapter 4

# Analysis and Discussion

## 4.1  SRIM Simulations for Optimization

In this section, we present simulation results for optimizing foil thickness and gas density, which are key parameters in improving AMS performance.

**Foil Thickness Optimization**

**Gas Density Optimization**

## 4.2  Isotopic Ratio Efficiency

## 4.3  Comparison of Degrader Foil and SiN Foil Stack Methods

We compare the efficiency of the degrader foil and SiN foil stack methods, focusing on their impact on detection efficiency and background suppression.

# Chapter 5

# Summary and Conclusion

This section summarizes the key findings of the study and discusses their implications for AMS-based $^{10}$Be detection

# Bibliography

[1] U. of Chicago, *What is carbon-14 dating?*, (2024) `https://news.uchicago.edu/explainer/what-is-carbon-14-dating`.

[2] G. Korschinek et al., "A new value for the half-life of $^{10}Be$ by heavy-ion elastic recoil detection and liquid scintillation counting", Nuclear Instruments and Methods in Physics Research Section B: Beam Interactions with Materials and Atoms **268**, 187–191 (2010), `https://doi.org/10.1016/j.nimb.2009.09.020`.

[3] J. Chmeleff et al., "Determination of the $^{10}$be half-life by multicollector icp-ms and liquid scintillation counting", Nuclear Instruments and Methods in Physics Research Section B: Beam Interactions with Materials and Atoms **268**, 192–199 (2010), `https://doi.org/10.1016/j.nimb.2009.09.012`.

[4] W. Ehmann and T. Kohman, "Cosmic-ray-induced radioactivities in meteorites—ii $^{26}Al$, $^{10}Be$ and $^{60}Co$, aerolites, siderites and tektites", Geochimica et Cosmochimica Acta **14**, 364–379 (1958), `https://doi.org/10.1016/0016-7037(58)90075-9`.

[5] P. Steier et al., "Comparison of methods for the detection of $^{10}$be with ams and a new approach based on a silicon nitride foil stack", International Journal of Mass Spectrometry **444**, 116175 (2019).

[6] E. A. Schuur, E. R. Druffel, and S. E. Trumbore, eds., *Radiocarbon and climate change: mechanisms, applications and laboratory techniques* (Springer, Dordrecht, 2013).

[7]   C. Tuniz et al., *Accelerator mass spectrometry: ultrasensitive analysis for global science* (CRC Press, Boca Raton, FL, 1998).

[8]   A. Steinhof, "Accelerator mass spectrometry of radiocarbon", *Radiocarbon and climate change*, edited by E. Schuur, E. Druffel, and S. Trumbore (Springer, Cham, 2016).

[9]   J. Olsen et al., "Radiocarbon analysis on the new aarams 1mv tandetron", Radiocarbon **59**, 905–913 (2017).

[10]  WebElements, *Copper*, 2024, https : / / www . webelements . com / copper/atoms.html.

[11]  J. E. McMurry, *Chemistry*, 8th ed. (Pearson, Year).

[12]  High Voltage Engineering Europa B.V., *Operator Manual 1.0 AMS System* (2013).

[13]  Wikipedia contributors, *Hall Effect Sensor — Wikipedia, The Free Encyclopedia*, 2024, https://en.wikipedia.org/wiki/Hall_effect_sensor.

[14]  Electronics Tutorials, *Hall effect and the hall effect sensor*, 2024, https : / / www . electronics - tutorials . ws / electromagnetism / hall-effect.html.

[15]  D. Weisser, "Stripper systems", *Electrostatic accelerators*, edited by R. Hellborg (Springer, Berlin Heidelberg, 2005), pp. 166–180.

[16]  National Museums of Scotland, *Cockcroft-walton generator*, (2022) https://www.nms.ac.uk/explore-our-collections/stories/science-and-technology/cockcroftwalton-generator.

[17]  G. Journals, *Grd journal article*, https://grdjournals.com/uploads/article/GRDJE/V01/I04/0125/GRDJEV01I040125.pdf.

[18]  M. Klein et al., "Extension of the hve 1 mv multi-element ams system for low background", Nuclear Instruments and Methods in Physics Research Section B **331**, 204–208 (2014).

[19]  H. J. Whitlow and H. Timmers, "Charge exchange and electron stripping", *Electrostatic accelerators*, edited by R. Hellborg (Springer, Berlin Heidelberg, 2005).

[20]  E. P. R. Møller, "Ams $^{14}canalyseatanaccelerationpotentialof600kv$", MA thesis (Aarhus University, 2022).

[21]  S. Kovalchuk, A. Dzhonov, and other authors, "Design of a faraday cup with slits for precise measurements of ion beams", Nuclear Instruments and Methods in Physics Research Section A **802**, 114–120 (2015), `https://www.sciencedirect.com/science/article/pii/S0168900215011675`.

[22]  P. Sigmund, *Particle penetration and radiation effects*, Vol. 151, Springer Series in Solid State Sciences (Springer-Verlag, Berlin Heidelberg, 2006).

[23]  M. M. Breunig et al., "Lof: identifying density-based local outliers", Proceedings of the acm sigmod 2000 international conference on management of data (2000), [insert page numbers here], `https://www.dbs.ifi.lmu.de/Publikationen/Papers/LOF.pdf`.

[24]  J. Olsen, *Cosmogenic isotope data analysis at aarams*, tech. rep., version 1.1 (Department of Physics and Astronomy, Aarhus University, 2017).

# Appendix A

# Appendices

Hello :)